

Block–spiral magnetism: An exotic type of frustrated order

J. Herbrych^{a,b,c,1} , J. Heverhagen^{d,e}, G. Alvarez^{f,g}, M. Daghofer^{d,e}, A. Moreo^{a,b} , and E. Dagotto^{a,b}

^aDepartment of Physics and Astronomy, University of Tennessee, Knoxville, TN 37996; ^bMaterials Science and Technology Division, Oak Ridge National Laboratory, Oak Ridge, TN 37831; ^cDepartment of Theoretical Physics, Faculty of Fundamental Problems of Technology, Wrocław University of Science and Technology, 50-370 Wrocław, Poland; ^dInstitute for Functional Matter and Quantum Technologies, University of Stuttgart, D-70550 Stuttgart, Germany; ^eCenter for Integrated Quantum Science and Technology, University of Stuttgart, D-70550 Stuttgart, Germany; ^fComputational Sciences and Engineering Division, Oak Ridge National Laboratory, Oak Ridge, TN 37831; and ^gCenter for Nanophase Materials Sciences, Oak Ridge National Laboratory, Oak Ridge, TN 37831

Edited by Andrew P. Mackenzie, Max Planck Institute for Chemical Physics of Solids, Dresden, Germany, and accepted by Editorial Board Member Angel Rubio May 15, 2020 (received for review January 20, 2020)

Competing interactions in quantum materials induce exotic states of matter such as frustrated magnets, an extensive field of research from both the theoretical and experimental perspectives. Here, we show that competing energy scales present in the low-dimensional orbital-selective Mott phase (OSMP) induce an exotic magnetic order, never reported before. Earlier neutron-scattering experiments on iron-based 123 ladder materials, where OSMP is relevant, already confirmed our previous theoretical prediction of block magnetism (magnetic order of the form $\uparrow\uparrow\downarrow\downarrow$). Now we argue that another phase can be stabilized in multiorbital Hubbard models, the block–spiral state. In this state, the magnetic islands form a spiral propagating through the chain but with the blocks maintaining their identity, namely rigidly rotating. The block–spiral state is stabilized without any apparent frustration, the common avenue to generate spiral arrangements in multiferroics. By examining the behavior of the electronic degrees of freedom, parity-breaking quasiparticles are revealed. Finally, a simple phenomenological model that accurately captures the macroscopic spin spiral arrangement is also introduced, and fingerprints for the neutron-scattering experimental detection are provided.

multiorbital Hubbard model | frustrated magnetism | Fe-based superconductors

Frustrated magnetism is one of the main areas of research in contemporary condensed-matter physics. In the generic scenario, magnetic frustration emerges from the failure of the system to fulfill simultaneously conflicting local requirements. As a consequence, complex spin patterns can develop from geometrical frustration (as in triangular, Kagome, or pyrochlore lattices) or from special spin–spin interactions (long-range exchange, Dzyaloshinskii–Moriya coupling, Kitaev model, spin-orbit effects, and others). In real materials both scenarios often coexist. Competing mechanisms can lead to interesting phenomena, such as spiral order (1–3), spin ice (4), skyrmions (5), spin liquids (6, 7), and resonating valence bond states (8). Also, the electronic properties of such systems are of much interest: It was shown that the interplay of a spiral state on a metallic host can support Majorana fermions (9–14) and can also induce multiferroicity (15–21).

Another example of competing interactions is the orbital-selective Mott phase (OSMP) (22, 23). In multiorbital systems, this effect can lead to the selective localization of electrons on some orbitals. The latter coexist with itinerant bands of mobile electrons. This unique mixture of localized and itinerant components in multiorbital systems could be responsible for the (bad) metallic behavior of the parent compounds of iron-based superconductors. This is in stark contrast to cuprates, usually described by the single-band Hubbard model, where parent materials are insulators. Furthermore, the OSMP can also host exotic magnetic phases. It was shown that the competition between Hund and Hubbard interactions can stabilize unexpected block magnetism (24–28), namely antiferromagnetically

(AFM)-coupled ferromagnetic (FM) islands. The size and shape of such islands depend on the electronic filling of the itinerant orbitals. This work focuses on two representative cases: 1) the $\pi/2$ -block spin-pattern $\uparrow\uparrow\downarrow\downarrow$ and 2) the $\pi/3$ -block spin-pattern $\uparrow\uparrow\downarrow\downarrow\downarrow$. Note that these block patterns are not spin-density waves: The local expectation values of spin operators yield uniform magnetization throughout the system, unlike a spin wave that would have peaks and valleys. Our study, on the other hand, indicates a clear block structure with spins of the same magnitude at each site (26–28). Moreover, exact diagonalization results on small lattices (27) indicate that the block-OSMP ground state has a large overlap (at least 50%) with a state of the form $|\uparrow\uparrow\downarrow\downarrow\rangle - |\downarrow\downarrow\uparrow\uparrow\rangle$ (as exemplified for the $\pi/2$ block). As a consequence, our states can be viewed as Néel-like states of an enlarged magnetic unit cell.

The OSMP was shown (22) to be relevant for the low-dimensional family of iron-based ladders, the so-called 123 family AFe_2X_3 , where $A = Ba, K, Rb$ is an alkaline earth metal and $X = S, Se$ is a chalcogen. From the magnetism perspective, two phases were experimentally reported: 1) For $BaFe_2Se_3$ inelastic neutron scattering (INS) identified (29) a 2×2 block–magnetic phase in a $\uparrow\uparrow\downarrow\downarrow$ pattern along the legs. Neutron diffraction

Significance

Magnetic frustration in spin or electronic models emerges from the failure of the system to fulfill simultaneously conflicting local requirements. The latter typically arise from the lattice geometry or are induced by special spin–spin interactions in the system at various distances. Here we show that the competing energy scales of the seemingly nonfrustrated orbital-selective Mott phase of the low-dimensional multiorbital Hubbard model can originate a “block–chiral magnetism,” i.e., a state with rigidly rotating spin–magnetic islands. Furthermore, we show how such an exotic spin state influences the electronic properties of the system, revealing parity-breaking quasiparticles.

Author contributions: J. Herbrych, M.D., A.M., and E.D. designed research; J. Herbrych and J. Heverhagen performed research; J. Herbrych, G.A., M.D., A.M., and E.D. contributed new reagents/analytic tools; J. Herbrych and J. Heverhagen analyzed data; and J. Herbrych, J. Heverhagen, G.A., M.D., A.M., and E.D. wrote the paper.

The authors declare no competing interest.

This article is a PNAS Direct Submission. A.P.M. is a guest editor invited by the Editorial Board.

Published under the [PNAS license](#).

Data deposition: Computer codes used in this study are available at <https://g1257.github.io/dmrgPlusPlus/>. All data discussed in this paper are available to readers at <https://g1257.github.io/papers/104/>.

¹To whom correspondence may be addressed. Email: jacek.herbrych@pwr.edu.pl.

This article contains supporting information online at <https://www.pnas.org/lookup/suppl/doi:10.1073/pnas.2001141117/-DCSupplemental>.

measurements and muon spin relaxation yield the same conclusion (30). 2) On the other hand, for BaFe₂S₃ and RbFe₂Se₃ INS reported (31–33) 2×1 blocks, FM along rungs and AFM along legs. Both of these phases are captured by the multiorbital Hubbard Hamiltonian (26) and also by its low-energy effective description (28), the generalized Kondo–Heisenberg model.

In this work, we unveil another magnetic phase that we stabilized; namely, we report an exotic block–spiral state. Such a state arises as a consequence of simultaneous tendencies in the system to form magnetic blocks and to develop noncollinear order. Different from standard spirals where one can observe spin-to-spin rotation, in the block–spiral state the blocks rigidly rotate, as illustrated in the three panels in Fig. 1A. The block–spiral states we report have similarities with states in the rare-earth material TbFeO₃ (34) that display spin incommensurability and domain walls. However, the length scales in TbFeO₃ are much larger, 340 Å, and magnetic fields or anisotropy are needed for their stabilization. Furthermore, the block–spiral magnetic pattern appears without any apparent frustration in the model and is a consequence of subtly competing energy scales present in the OSMP. This spin order originates in ferromagnetic tendencies, induced by Hund physics in multiorbital systems, and opposite antiferromagnetic superexchange tendencies, caused by Hubbard interactions. There is a hidden frustration in the system, not obvious at the Hamiltonian level, and whose exotic consequences appear only when powerful computational tools are used: Simpler biased techniques likely would have missed this state. We propose two simpler phenomenological models that capture the essence of our findings. Moreover, the electronic properties can be accurately described by quasiparticles that break parity sym-

metry, as expected within a spiral state. Also, we show that the behavior of spins can be effectively modeled via a frustrated long-range spin-only Heisenberg model. Such a spin model can serve as a starting point for the spin-wave theory calculations often used to compare theory vs. INS spectra. Our findings are robust against system parameter changes and should characterize generic multiorbital systems in the OSMP regime, close to ferromagnetism.

Results

Magnetism of OSMP. We discuss the properties of a multiorbital Hubbard model on a one-dimensional (1D) lattice. In the generic SU(2)-symmetric form it can be written as

$$H_H = - \sum_{\gamma, \gamma', \ell, \sigma} t_{\gamma\gamma'} \left(c_{\gamma, \ell, \sigma}^\dagger c_{\gamma', \ell+1, \sigma} + \text{H.c.} \right) + \Delta \sum_{\ell} n_{1, \ell} + U \sum_{\gamma, \ell} n_{\gamma, \ell, \uparrow} n_{\gamma, \ell, \downarrow} + (U - 5J_H/2) \sum_{\ell} n_{0, \ell} n_{1, \ell} - 2J_H \sum_{\ell} \mathbf{S}_{0, \ell} \cdot \mathbf{S}_{1, \ell} + J_H \sum_{\ell} \left(P_{0, \ell}^\dagger P_{1, \ell} + \text{H.c.} \right). \quad [1]$$

Here, $c_{\gamma, \ell, \sigma}^\dagger$ ($c_{\gamma, \ell, \sigma}$) creates (destroys) an electron with spin projection $\sigma = \{\uparrow, \downarrow\}$ at orbital $\gamma = \{0, 1\}$ of site $\ell = \{1, \dots, L\}$. Δ stands for crystal-field splitting, while $n_{\gamma, \ell} = \sum_{\sigma} n_{\gamma, \ell, \sigma}$ represents the total density of electrons at (γ, ℓ) , with $n_{\gamma, \ell, \sigma}$ as the density of electrons with σ -spin projection. U is the standard, same-orbital repulsive Hubbard interaction, and J_H is the Hund exchange between spins $\mathbf{S}_{\gamma, \ell}$ at different orbitals γ . Finally, the last term $P_{0, \ell}^\dagger P_{1, \ell}$ stands for pair hopping between orbitals, where $P_{\gamma, \ell} = c_{\gamma, \ell, \uparrow} c_{\gamma, \ell, \downarrow}$.

In the most generic case, the Fe-based materials should be modeled with five 3d orbitals (three t_{2g} , d_{xy} , d_{yz} , d_{xz} ; and two e_g , $d_{x^2-y^2}$, d_{z^2}). However, it is widely believed (35, 36) that the t_{2g} orbitals are the most relevant orbitals close to the Fermi surface. Furthermore, the d_{yz} and d_{xz} orbitals are often (or are close to being) degenerate and, as a consequence, one can design (28) two-orbital models. Such a choice represents a generic case of coexisting wide and narrow electronic bands, as often found in iron-based materials from the 123 family (23, 26, 37–39). The particular choice of the hopping matrix elements $t_{\gamma\gamma'}$ used here—specifically $t_{00} = -0.5$ [eV], $t_{11} = -0.15$ [eV], and $t_{01} = t_{10} = 0$ —and crystal-field splitting $\Delta = 0.8$ [eV] is motivated by several previous studies (26–28) on the magnetic properties of the OSMP. The above values yield a kinetic energy bandwidth $W = 2.1$ eV which is used as an energy unit throughout this paper. Finally, to reduce the number of parameters of the Hamiltonian the value of Hund exchange is fixed to $J_H = U/4$ throughout our investigation. The rationale behind this value comes from dynamical mean-field theory (using local-density approximation) calculations and is believed to be experimentally relevant (40–42). Also, it was shown (43) that in a wide range of Hund couplings, the OSMP properties are the same (26, 43).

It was previously shown (28) that the magnetic properties of the OSMP can be qualitatively, and even quantitatively, described by the effective Hamiltonian obtained by Schrieffer–Wolff transforming the subspace with strictly one electron per site at the localized orbital $\gamma = 1$, leading to the generalized Kondo–Heisenberg (gKH) model

$$H_K = -t_{00} \sum_{\ell, \sigma} \left(c_{0, \ell, \sigma}^\dagger c_{0, \ell+1, \sigma} + \text{H.c.} \right) + U \sum_{\ell} n_{0, \ell, \uparrow} n_{0, \ell, \downarrow} + K \sum_{\ell} \mathbf{S}_{1, \ell} \cdot \mathbf{S}_{1, \ell+1} - 2J_H \sum_{\ell} \mathbf{S}_{0, \ell} \cdot \mathbf{S}_{1, \ell}, \quad [2]$$

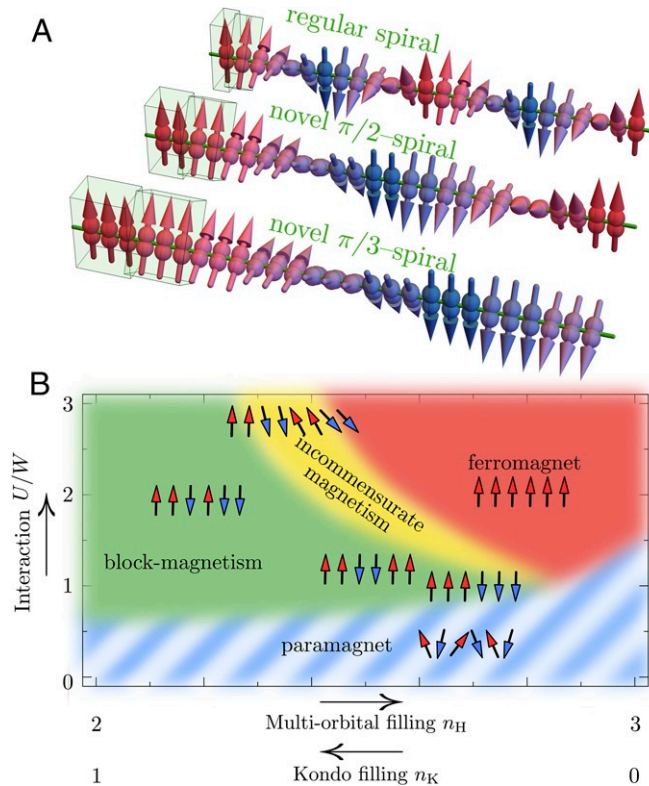


Fig. 1. Schematic representation of spirals within the orbital-selective Mott phase. (A) Top to Bottom: standard spiral spin structure with site-to-site spins rotation and block–spirals of two and three sites, respectively. (B) Interaction U -filling $n_{H/K}$ phase diagram. Solid (striped) coloring represents the OSMP (paramagnetic) region.

where $K = 4t_{11}^2/U$. It is worth noting that due to particle-hole symmetry, the electronic filling relation between the two-orbital Hubbard (n_H) and gKH (n_K) models is $n_K = 3 - n_H$.

In this work, we primarily reach our conclusions on the basis of the gKH Hamiltonian, Eq. 2. However, in [SI Appendix](#) we reproduce the main findings with the full two-orbital Hubbard model Eq. 1. All Hamiltonians are diagonalized via the single-site density matrix renormalization group (DMRG) method (44–47) (with up to 1,200 states kept), where the dynamical correlation functions are obtained using the dynamical-DMRG technique (48–50), i.e., calculating spectral functions directly in frequency space with the correction-vector method (51) and Krylov decomposition (50). Open boundary conditions are assumed.

Let us briefly describe the several magnetic phases of the OSMP, where the phase reported here is in yellow in Fig. 1B. For details we refer the interested reader to ref. 28. In Fig. 1B we present a sketch of the interaction-filling (U - $n_{H/K}$) phase diagram: 1) At $U < W$ the ground state is a paramagnetic metal. 2) For $U \gtrsim W$ the system enters the OSMP with coexisting metallic and Mott-insulating bands. 3) For sufficiently large values of interaction $U \gg W$ the system is in a FM state for all fillings. 4) When $U \sim \mathcal{O}(W)$, namely when all energy scales compete, the system is primarily in the so-called block-magnetic state. Depending on the filling of the itinerant band, the spins form various sizes of AFM-coupled FM spin islands. An important special case, found experimentally in BaFe_2Se_3 , is the $n_K = 1/2$ ($n_H = 3/2 + 1$) filling where spins form a $\uparrow\uparrow\downarrow\downarrow\uparrow\uparrow\downarrow\downarrow$ pattern along the legs, the $\pi/2$ -block magnetic state.

The Fourier analysis of the perfect step-function pattern of the form $\uparrow\uparrow\downarrow\downarrow\uparrow\uparrow\downarrow\downarrow$ yields only one Fourier mode at $\pi/2$, as shown in Fig. 2A. Our explicit DMRG calculations of the gKH spin structure factor $S(q) = \langle \mathbf{S}_q \cdot \mathbf{S}_{-q} \rangle$ [$\mathbf{S}_q = (1/\sqrt{L}) \sum_{\ell} \exp(-iq\ell) \mathbf{S}_{\ell}$ with $\mathbf{S}_{\ell} = \sum_{\gamma} \mathbf{S}_{\gamma,\ell}$] at $U \sim W$ confirms that the dominant contribution to the magnetic ordering indeed originates in a $\pi/2$ -block pattern. Equivalently, the analysis of a perfect $\uparrow\uparrow\downarrow\downarrow\uparrow\uparrow\downarrow\downarrow$ pattern yields now two equal-height Fourier components at $\pi/3$ and π . Calculations within gKH (Fig. 2A) display a large, dominant peak at $\pi/3$ but also a smaller one at π . The small weight of the latter can be explained by the emergence of optical modes of localized spin excitations present within multi-orbital systems (27). These modes manifest in $S(q)$ as a finite offset at large values of the wavevector (Fig. 2B). Nevertheless, the dominant shape of the block magnetism of the OSMP can be qualitatively described by idealized Heaviside-like patterns. The small size of our blocks shows that they cannot be characterized as domain walls that are usually separated by much larger distances, but as a different magnetic order.

Block-Spiral State and Chirality Correlation. In between the block and FM phases, we discovered a region where the spin static structure factor $S(q)$ has its maximum q_{\max} at incommensurate values of the wavevector q . In Fig. 3A and D we explicitly show the interaction U dependence of $S(q)$ in this region (28) for $n_K = 1/2$ and $n_K = 1/3$, respectively. It is evident from the presented results that the maximum of the spin structure factor continuously changes with interaction U interpolating between block magnetism at $U \sim W$ and the FM state at $U \gg W$ (e.g., at fixed $n_K = 1/2$, from $q_{\max} = \pi/2$ to $q_{\max} = 0$). The real-space spin-spin correlation functions $\langle \mathbf{S}_{L/2} \cdot \mathbf{S}_{\ell} \rangle$ (Fig. 3B and E) reveal an oscillatory structure throughout the chain, with period $\theta = q_{\max}$, decaying in amplitude at large spatial separations, within the incommensurate region in the phase diagram. Such behavior may naively suggest a spin-density wave. For the latter, the Fourier transform of the spin correlations should yield only one Fourier mode, due to $\langle \mathbf{S}_{L/2} \cdot \mathbf{S}_{\ell} \rangle \propto \cos(q_{\max}\ell)$. As we will show, this interpretation is incorrect and the competing interactions present in OSMP systems, as well as the location of this phase

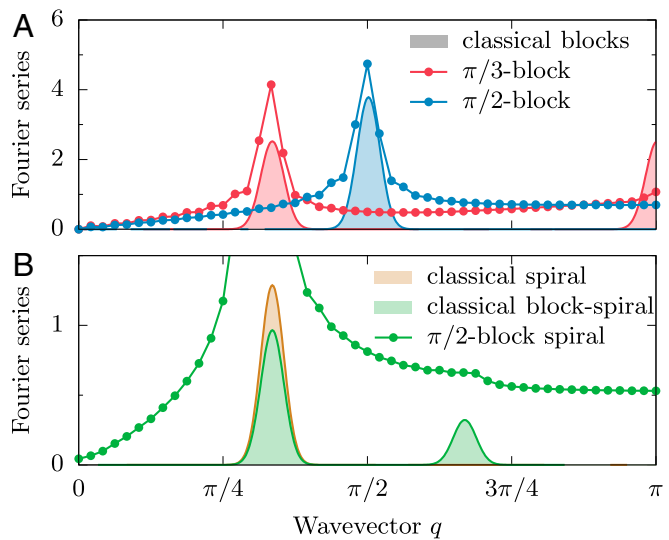


Fig. 2. Fourier decomposition of the spin order. (A) Analysis of classical Heaviside-like block patterns (shaded area), i.e., $\uparrow\uparrow\downarrow\downarrow$ and $\uparrow\uparrow\downarrow\downarrow\downarrow$. Line dots represent the corresponding calculations using the generalized Kondo-Heisenberg model at $U = W$, $n_H = 1/2$, and $n_H = 1/3$ ($\pi/2$ and $\pi/3$ blocks, respectively). (B) Shaded areas represent 1) perfect standard spiral with one Fourier mode and 2) our perfect block-spiral pattern displaying two modes. Line dots are DMRG results for the block-spiral order at $U/W = 1.95$ and $n_H = 0.5$. All results have pitch angle $\theta \simeq 1/3$. The shoulder in the DMRG data is the fingerprint of the block-spiral. Note that in all panels we have broadened the δ peaks of classical solutions for clarity.

sandwiched between block and FM states, lead to a block-spiral spin state.

To better investigate the magnetic structure of the spiral within the OSMP we focus on the chirality correlation function $\langle \boldsymbol{\kappa}_{\ell}^d \cdot \boldsymbol{\kappa}_m^d \rangle$ (2, 3, 52, 53), where

$$\boldsymbol{\kappa}_{\ell}^d = \mathbf{S}_{\ell} \times \mathbf{S}_{\ell+d} \quad [3]$$

represents the vector product of two spin operators separated by a distance d and consequently the angle between them. We stress that in the following we consider the total spin at each site $\mathbf{S}_{\ell} = \sum_{\gamma} \mathbf{S}_{\gamma,\ell}$. In the generic case of AFM or FM order, and also in the OSMP block phase, the chirality correlation function vanishes, $\langle \boldsymbol{\kappa}_{\ell}^d \cdot \boldsymbol{\kappa}_m^d \rangle = 0$, since the spins are collinear. On the other hand, consecutive $\langle \boldsymbol{\kappa}_{\ell}^d \cdot \boldsymbol{\kappa}_m^d \rangle \neq 0$ indicates a nontrivial spiral order.

In Fig. 3C and F we present the interaction U dependence of the nearest-neighbor, $d = 1$, chirality correlation function $\langle \boldsymbol{\kappa}_{\ell}^1 \cdot \boldsymbol{\kappa}_m^1 \rangle$ of the gKH model. It is evident from the presented results that between the block and FM phases the chirality acquires finite values. In addition, the spatial structure of $\langle \boldsymbol{\kappa}_{\ell}^1 \cdot \boldsymbol{\kappa}_m^1 \rangle$ displays a clear zig-zag-like pattern. To better investigate the spiral internal structure, in Fig. 4 we present the dependence of the chirality correlation with the distance d between spins. In [SI Appendix](#) we provide the full interaction U dependence of the next-nearest-neighbor, $d = 2$, chirality correlation function. Here, as illustration we focus on the representative cases of $U/W = 2.0$ for $n_K = 1/2$ and $U/W = 1.2$ for $n_K = 1/3$.

As already mentioned, the nearest-neighbor ($d = 1$) chiral correlation for both considered fillings contains additional patterns modulating the usual decay. Specifically, for $n_K = 1/2$ ($n_K = 1/3$) the correlation function oscillates every two (three) sites. Interestingly, these patterns change their nature when the next-nearest-neighbor ($d = 2$) chirality is considered: 1) The values of these chiralities increase $\langle \boldsymbol{\kappa}_{\ell}^2 \cdot \boldsymbol{\kappa}_m^2 \rangle > \langle \boldsymbol{\kappa}_{\ell}^1 \cdot \boldsymbol{\kappa}_m^1 \rangle$, and 2) for the case of $n_K = 1/2$ the $\boldsymbol{\kappa}$ correlation is now a smooth function of distance, while $n_K = 1/3$ still exhibits some three-site

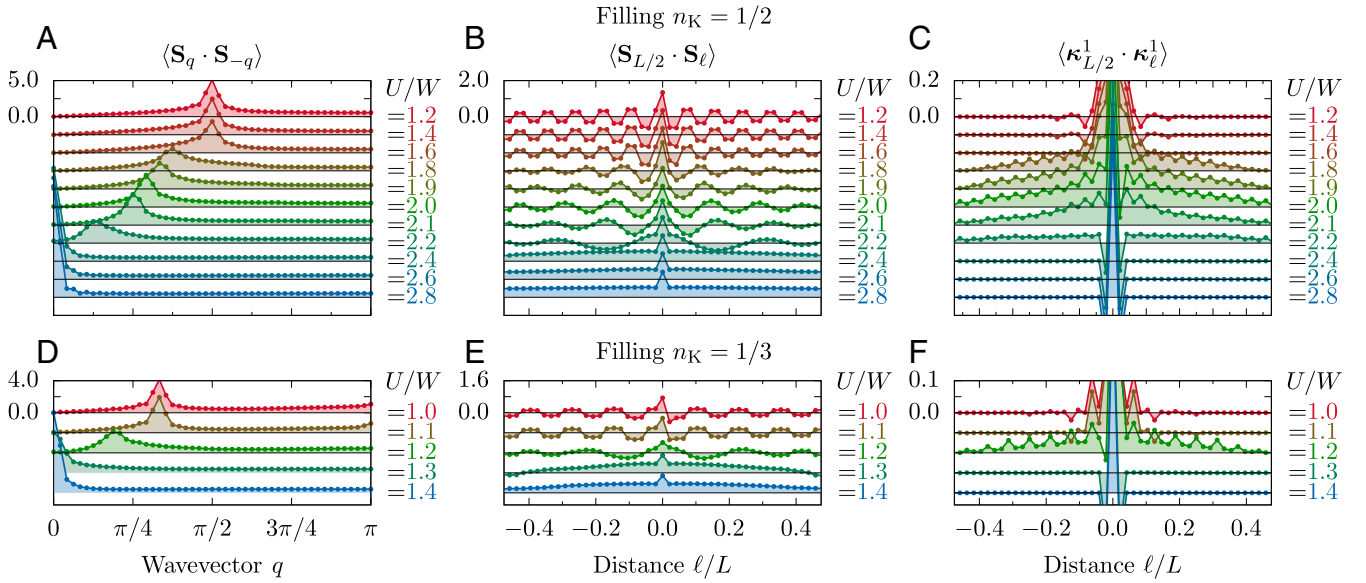


Fig. 3. Interaction U/W dependence of correlation functions. (A and D) Static spin structure factor $\langle \mathbf{S}_q \cdot \mathbf{S}_{-q} \rangle$. (B and E) Real-space spin-spin correlation function $\langle \mathbf{S}_{L/2} \cdot \mathbf{S}_\ell \rangle$. (C and F) Nearest-neighbor chirality correlation function $\langle \kappa_{L/2}^1 \cdot \kappa_\ell^1 \rangle$. A–C represent results for filling $n_K = 1/2$, while D–F depict results for $n_K = 1/3$. All results were calculated using the DMRG and the generalized Kondo–Heisenberg model on $L = 48$ sites.

oscillations. Investigating the next–next–nearest-neighbor case, $d = 3$, gives additional information. While for the $n_K = 1/2$ filling the $d = 3$ correlations are smaller than $d = 1$ and $d = 2$, for $n_K = 1/3$ they are larger and (as for $d = 2$ at $n_K = 1/2$) they are now a smooth function of distance. This seemingly erratic behavior of $\langle \kappa_\ell^d \cdot \kappa_m^d \rangle$ correlations varying d cannot be simply explained by a mere uniform change of the pitch angle θ . The latter changes only with the interaction $\theta = \theta(U)$. On the other hand, as evident from Fig. 3 C and F, the internal structure of $\langle \kappa_\ell^1 \cdot \kappa_m^1 \rangle$ depends only on the electronic filling n_K (see also SI Appendix for $d = 2$ results).

To better explain this behavior let us focus on the dimer correlation defined (54) as

$$D_{\pi/2} = \frac{2}{L} \sum_{\ell=L/4}^{3L/4} (-1)^{\ell-1} \langle \mathbf{S}_\ell \cdot \mathbf{S}_{\ell+1} \rangle. \quad [4]$$

The above operator compares the number of FM and AFM bonds in the bulk of the system (SI Appendix contains the full real-space dependence of $\langle \mathbf{S}_\ell \cdot \mathbf{S}_{\ell+1} \rangle$). For true FM or AFM ordered states, $|\uparrow\uparrow\uparrow\uparrow\dots\rangle$ or $|\uparrow\downarrow\uparrow\downarrow\dots\rangle$, respectively, each nearest-neighbor bond has the same sign: positive for FM $\uparrow\uparrow$ and negative for AFM $\uparrow\downarrow$. Consequently, $D_{\pi/2} = 0$. On the other hand, in the $\pi/2$ -block state, $|\uparrow\uparrow\downarrow\downarrow\dots\rangle$, the FM and AFM bonds alter in staggered fashion, rendering $D_{\pi/2} \neq 0$. In Fig. 5 we present the interaction U dependence of $D_{\pi/2}$ for $n_K = 1/2$. Furthermore, in Fig. 5 we present also the wavevector where the static structure factor is maximized, q_{\max} , and the value of the $\tilde{\kappa}_{L/3}^d = \langle \kappa_\ell^d \cdot \kappa_m^d \rangle_{|\ell-m|=L/3}$ correlator for $d = 1$ and $d = 2$. Starting in the paramagnet at small U both $D_{\pi/2}$ and $\tilde{\kappa}_{L/3}^d$ vanish, with $q_{\max} = \pi$ just depicting the usual short-range staggered correlations of weak- U physics. In the opposite limit of strong interaction, $U \gg W$, $D_{\pi/2} = \tilde{\kappa}_{L/3}^d = 0$ as well, a consequence of a simple FM state with $q_{\max} = 0$. In the most interesting case of competing interaction $U \sim W$, the dimer correlation $D_{\pi/2}$ acquires a finite value maximized at $U \simeq W$. The latter reflects a perfect $\pi/2$ -block magnetic state. Interestingly, one can observe a continuous transition of $D_{\pi/2}$ between the block and FM

phases in the region where a finite chirality $\tilde{\kappa}_{L/3}^d \neq 0$ was found and where q_{\max} takes incommensurate values.

On the basis of the above results, a coherent picture emerges explaining the nature of the magnetic state between the block and FM limits. Consider first filling $n_K = 1/2$. At $U \simeq W$ the ground state is a block–magnetic phase, where two-site FM islands (blocks) are AFM coupled. Increasing the interaction U , the spins start to rotate with respect to each other, inducing finite

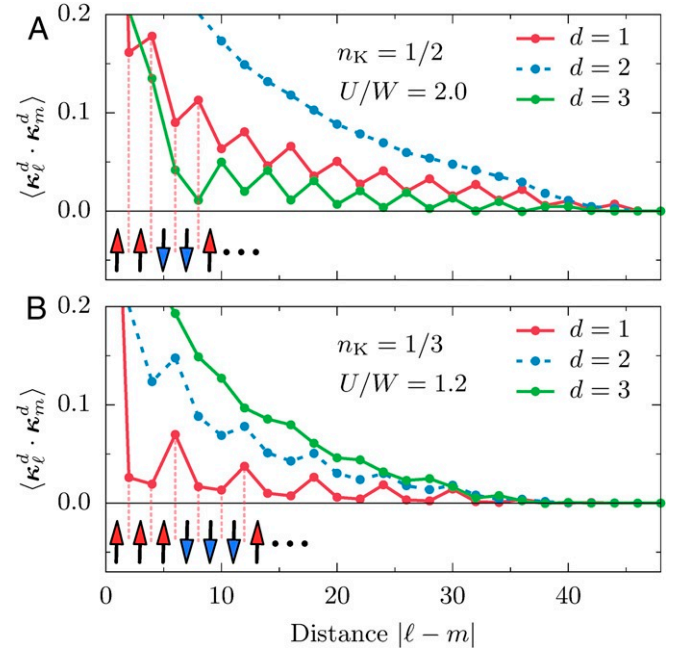


Fig. 4. Chiral correlation function $\langle \kappa_\ell^d \cdot \kappa_m^d \rangle$. (A) Dependence of chirality $\kappa_\ell^d = \mathbf{S}_\ell \times \mathbf{S}_{\ell+d}$ on distance d between spins. Results were calculated using the generalized Kondo–Heisenberg model, $L = 48$, $n_K = 1/2$, and $U/W = 2.0$. (B) Same as A but for $n_K = 1/3$ and $U/W = 1.2$. In both A and B arrows represent schematics of the block order for given filling.

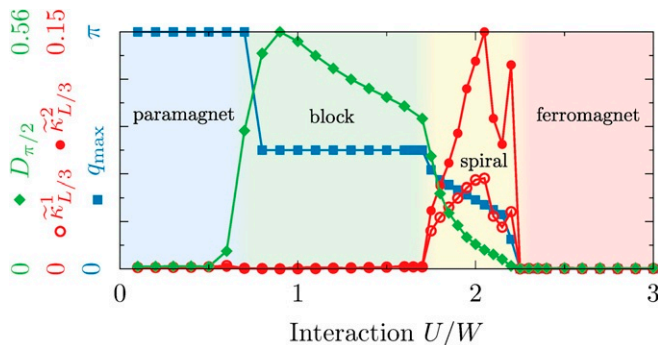


Fig. 5. Phase diagram varying the interaction U/W . Presented are 1) maximum of static spin structure factor q_{\max} (squares), 2) nearest-neighbor ($d=1$) and next-nearest-neighbor ($d=2$) chirality $\tilde{\kappa}_{L/3}^d$ (open and solid circles, respectively), and 3) dimer correlation $D_{\pi/2}$ (diamonds). Results were calculated using the generalized Kondo–Heisenberg model, $L=48$ sites, and $n_{\kappa}=1/2$.

$\langle \kappa_{\ell}^d \cdot \kappa_m^d \rangle$ correlations. Remarkably, during the rotation the overall FM islands-nature of the state is preserved, yielding a finite $D_{\pi/2} \neq 0$ all of the way to the FM state at $U \gg W$. Such an unexpected scenario is also encoded in the inequalities $\tilde{\kappa}_{L/3}^2 > \tilde{\kappa}_{L/3}^1$ and $\tilde{\kappa}_{L/3}^2 > \tilde{\kappa}_{L/3}^3$ observed in Fig. 4A. This is qualitatively different from a standard spiral state where the spin rotates from site to site (Fig. 1A, *Top* sketch). In our case, instead, the spiral is made of individual blocks, and it is the entire block that rotates from block to block (Fig. 1A, *Middle* sketch). Furthermore, the detailed analysis of $S(q)$ reveals a small secondary Fourier mode at $\pi - q_{\max}$ (Fig. 2B). As already mentioned, the long-wavelength components of $S(q)$ are hidden behind the OSMP optical mode contribution (27) and a detailed analysis of experimental dynamical spin spectra will be needed to fully reveal the presence of our predicted block–spiral states. Because these additional modes are not consistent with a mere standard spiral but instead appear in the Fourier analysis of the perfectly sharp block $\uparrow\uparrow\downarrow\downarrow$ state modulated by the spiral \cos -like component and are also consistent with our analysis of $\tilde{\kappa}$, they represent the fingerprints of our block–spiral states.

Such a block–spiral state can also be observed at filling $n_{\kappa}=1/3$. Here, $\pi/3$ blocks of three sites $\uparrow\uparrow\downarrow\downarrow$ develop a finite dimer correlation of the form $D_{\pi/3} \propto \sum_{\ell} f(\ell) \langle \mathbf{S}_{\ell} \cdot \mathbf{S}_{\ell+1} \rangle$, where $f(\ell)$ accounts for the specific form of the bond sign pattern, i.e., $\{1, 1, -1, 1, 1, -1, \dots\}$ (SI Appendix). A finite $D_{\pi/3}$ together with $\tilde{\kappa}_{L/3}^3 > \tilde{\kappa}_{L/3}^2 > \tilde{\kappa}_{L/3}^1$ is compatible with a spiral state of rotating three-site blocks (Fig. 1A, *Bottom* sketch).

Finally, let us comment on the finite-size dependence of our findings. Analysis of system sizes up to $L=96$ sites (SI Appendix) indicates that the discussed block–spiral states display short-ranged order but with a robust correlation length of $\xi \sim 15$ sites, where $\langle \kappa_{\ell}^d \cdot \kappa_{\ell+x}^d \rangle \propto \exp(-x/\xi)$. However, it was argued (2, 55) for the case of the FM long-range Heisenberg model that realistic small $SU(2)$ -breaking anisotropies, often present in real materials, can induce true (quasi-)long-range order in a spiral state. Also, such an anisotropy will choose the plane of rotation of the spiral, i.e., in plane or out of plane with regard to the chain direction. As we argue in the next section, such (frustrated) long-range Heisenberg Hamiltonians can (at least qualitatively) capture the main physics of the block–spiral unveiled here.

We emphasize that the same conclusions are reached in the multiorbital Hubbard model, although because the effort is much more computationally demanding, it was limited to spe-

cial cases. In SI Appendix we present results for $\langle \kappa_{\ell}^d \cdot \kappa_m^d \rangle$ obtained with the full two-orbital Hubbard model Eq. 1 and also the incommensurability of $S(q)$ for a three-orbital Hubbard model.

Quasiparticle Excitations. A distinctive feature of the OSMP is the coexistence of localized electrons (spins in an insulating band) and itinerant electrons (a metallic band). In the block–magnetic phase at $U \simeq W$ it was previously shown (39)—for the three-orbital Hubbard model—that the density of states (DOS) at the Fermi level ϵ_F is reduced, indicating a pseudogap-like behavior. Our calculations of the single-particle spectral function $A(q, \omega)$ and $DOS(\omega)$ (SI Appendix) using the gKH model are presented in Fig. 6A and confirm this picture. They also show the strength of our effective Hamiltonian: The behavior of the gKH model perfectly matches the $\gamma=0$ itinerant orbital of the full two-orbital Hubbard result presented in Fig. 6C. It is worth noting that to properly match the electron and hole parts of $A(k, \omega)$ between the models we exploit the particle–hole symmetry of gKH and present results for $n_{\kappa}=3/2$ (instead of $n_{\kappa}=1/2$ for which the spectrum would be simply mirrored, i.e., $\omega \rightarrow -\omega$ and $k \rightarrow \pi - k$). Also, we reiterate here that although the system is overall metallic in nature, the band structure is vastly different from the simple cosine-like result of $U \rightarrow 0$. Distinctive features in $A(q, \omega)$ at the Fermi vector k_F , and a large renormalization of the overall band structure at higher energies, indicate a complex interplay between various degrees of freedom and energy scales.

Upon increasing the interaction U and entering the block–spiral region, $A(q, \omega)$ changes drastically. In Fig. 6B we show representative results for a $\theta/\pi \simeq 0.3$ block–spiral state at $U/W=2$ and $n_{\kappa}=1/2$. Two conclusions are directly evident from the presented results: 1) The pseudogap at ϵ_F is closed, but some additional gaps at higher energies opened. 2) $A(q, \omega)$ in the vicinity of the Fermi level, $\omega \sim \epsilon_F$, develops two bands, intersecting at the $q=0$ and $q=\pi$ points, with maximum at $q \simeq \theta/2$. The bands represent two quasiparticles: left and right movers reflecting the two possible rotations of the spirals. It is obvious from the above results that the quasiparticles break the parity symmetry; i.e., going from $q \rightarrow -q$ momentum changes the quasiparticle character, as expected for a spiral state. Somewhat surprisingly, $A(q, \omega)$ does not show any gap as would typically be associated with the finite dimerization D_{α} that we observe. However, it should be noted that for quantum localized $S=1/2$ spins the quarter-filling ($n_{\kappa}=1/2$) implies a filling of two-fifths of the lower Kondo band (due to the energy difference between local Kondo singlets and triplets). The dimerization gap expected at $\pi/2$ would thus open away from the Fermi level and would consequently not confer substantial energy gain to the electrons. Similarly, no dimerization gap is found in the $n_{\kappa} \simeq 0.33$ case, i.e., the $\pi/3$ -block–spiral (not presented). We thus conclude that quantum fluctuations of the localized and itinerant spins are here strong enough to suppress the dimerization gap. The above conclusions can be also reached from results obtained with the full two-orbital Hubbard model (Fig. 6D).

Discussion and Effective Model

It was previously shown (27) that the frustrated FM-AFM J_1 - J_2 Heisenberg model (with $|J_1| \sim J_2$) qualitatively captures the physics of the nonspiral block–magnetic state. Here, in Fig. 7A we show that the spin structure factor $S(q)$ of the block–spiral state can be accurately described by an extension of that model: the frustrated long-range Heisenberg Hamiltonian. Although this phenomenological model is not derived here from the basic Hamiltonians, it accurately reproduces the interaction U dependence throughout the incommensurate region (e.g., compare Figs. 3A and 7B). The intuitive understanding of the origin of the effective spin model is as follows: At $U \sim W$ the system

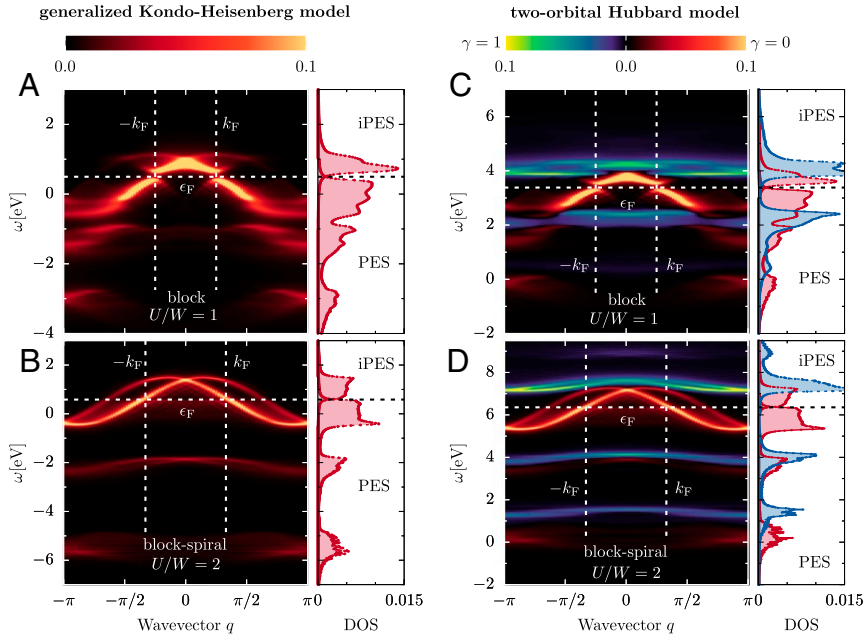


Fig. 6. Spectral function $A(q, \omega)$. (A and B) Block phase ($n_K = 3/2, U/W = 1.0$) (A) and block-spiral phase ($n_K = 3/2, U/W = 2.0$) (B) as calculated for the generalized Kondo-Heisenberg model using $L = 48$ sites. (C and D) The same results obtained with the two-orbital Hubbard model ($L = 48$). (C) Block phase ($n_H = 2.50, U/W = 1.0$). (D) block-spiral phase ($n_H = 2.50, U/W = 2.0$). (A–D) Horizontal (vertical) lines depict the Fermi level ϵ_F (Fermi wavevector k_F), while (i)PES stands for (inverse-) photoemission spectroscopy. (A–D, Right) Density of states $\text{DOS}(\omega) = \sum_q A(q, \omega)$.

is in a block-magnetic state with quasi-long-range (QLR) spin correlation of π/N_b nature, where N_b is the size of the block. We found excellent agreement between the gKH and Heisenberg models with $J_1 = -1, J_2 = 1/4, J_3 = 1/10$ (see also Fig. 7A, *Inset* for the J_2 - J_3 dependence of q_{max}). The latter yields $\alpha \simeq 2$ in $|J_r| \propto 1/r^\alpha$. As a consequence, the block-spiral magnetism is described by the class of Haldane-Shastry models (56, 57). In fact, we speculate that due to the oscillating character of the electron-mediated exchange couplings, the spin system which encompasses all phenomena is given by

$$H = \sum_{\ell, r} J_r \mathbf{S}_\ell \cdot \mathbf{S}_{\ell+r},$$

$$\text{with } J_1 < 0, \quad J_2 > 0, \quad J_{r>2} = |J_1| \frac{(-1)^{r-1}}{r^\alpha}. \quad [5]$$

It was shown (58–60) that the above model has (for the zero-magnetization sector, $S_{\text{tot}}^z = 0$) a QLR ground state with $\pi/2$ correlations and also can support spiral states. Such frustrated long-range Hamiltonians are not suitable for direct DMRG calculations due to the area law of entanglement. Thus, alternatively in SI Appendix we show small system size Lanczos diagonalization results for Eq. 5. However, as presented in Fig. 7, the first three terms J_1 - J_2 - J_3 (which can still be computed accurately with DMRG) already give satisfactory results even for the chirality correlator (compare Figs. 3C and 7C).

Finally, we make two additional comments: 1) The scenario (long-range effective spin model) described above goes beyond the discussed nonspiral $\pi/2$ -block case. Changes in the magnetization sector of the long-range FM Hamiltonian lead to modifications in the periodicity of the QLR order (61, 62). As a consequence, there are only a few parameters in the effective spin model: the magnetization S_{tot}^z related to the filling in the original full multiorbital Hamiltonian and $\{J_2, \alpha\} = f(U)$ which controls the long-range nature of the system. 2) Since our system is overall metallic (albeit likely a bad metal because of the localized component), one could naively believe that

the Ruderman-Kittel-Kasuya-Yosida (RKKY) spin exchange J_r carried by mobile electrons could explain some of our results. However, this is not the case because the nontrivial effect of the interaction U —creating a metallic state coexisting with a (quasi)ordered magnetic state—qualitatively modifies the nature of the RKKY interaction.

Conclusion

We have identified the block-spiral magnetism in which FM islands rigidly rotate with respect to each other. We emphasize the crucial role of correlation in this phenomenon. Spiral states are usually a consequence of frustration (geometrical or induced by competing interactions) or of explicit symmetry-breaking terms like Dzyaloshinskii-Moriya couplings. For example, long-period helical spin-density waves were reported (63–66) in many transition-metal compounds and rare-earth magnets. This is also the case for the hexagonal perovskite CsCuCl_3 , where the external magnetic field can induce block-like structure on top of the spiral-like order (67). However, in all of these cases the magnetic structure resembles a domain wall and originates in strong frustration of the (often classical) model itself. On the contrary, in our system we have only nearest-neighbor interactions on a chain geometry, and the $\text{SU}(2)$ symmetry is preserved. Instead, the block-spiral state reported here appears as an effect of hidden frustration, i.e., competition between the double-exchange-like mechanism present in multiorbital systems dominated by a robust Hund exchange and the interaction U that governs superexchange tendencies. These nontrivial effects become apparent in the exotic effective (phenomenological) spin model we unveiled: a long-range frustrated Heisenberg model. Within the latter the spin exchange decays slowly with distance, $\sim 1/r^2$, in contrast to the usual RKKY interaction which decays faster. Also, to our knowledge the multiorbital system discussed in this work—as realized in iron-based compounds from the 123 family—could be one of the few, if not the only, known realizations of a Haldane-Shastry-like model with $\alpha = 2$.

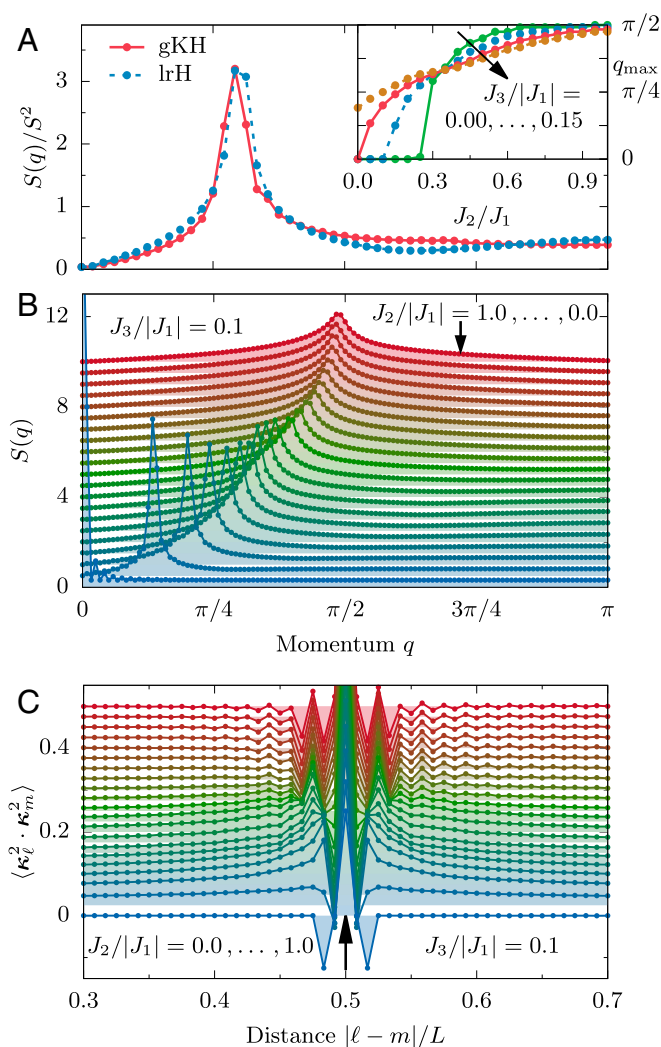


Fig. 7. Effective Heisenberg model. (A) Comparison of $S(q)$ between the gKH model in the spiral state ($L = 48$, $n_K = 1/2$, $U/W = 2.0$) and the long-range Heisenberg (IrH) model ($L = 48$, $J_2/|J_1| = 0.25$, $J_3/|J_1| = 0.1$). Note results are normalized by the magnetic moment $S^2 = \mathbf{S}(\mathbf{S} + 1)$; i.e., $S^2 = 1.375$ and $S^2 = 3/4$ for gKH and IrH, respectively. (B and C) Static spin structure factor $S(q)$ (B) and chirality correlation function $\langle \kappa_\ell^d \cdot \kappa_m^d \rangle$ (C) of the J_1 - J_2 - J_3 Heisenberg model (with ferromagnetic $J_1 = -1$), calculated for $L = 120$ sites, $J_3/|J_1| = 0.1$, and various $J_2/|J_1| = 0.00, 0.05, \dots, 1.00$ (top to bottom). (A, Inset) Position of the maximum of the static structure factor q_{\max} of the IrH model as a function of $J_2/|J_1|$, for $J_3/|J_1| = 0.00, 0.05, 0.10$, and 0.15 .

Furthermore, due to properties unique to the OSMP, primarily the coexistence of metallic and insulating bands, the block-spiral state displays exotic behavior in the electronic degrees of freedom. For example, new quasiparticles appear due to the parity breaking of the spiral state (left and right movers). Similar

physics can be found in systems with spin-orbit coupling (68, 69). Here, again, this is an effect of competing energy scales. Another interesting possibility is the existence of multiferroic behavior in our system. It is known (17–21) that in materials such as quasi-1D compounds LiCu_2O_2 , LiCuVO_2 , or $\text{PbCuSO}_4(\text{OH})_2$, the spin spirals drive the system to ferroelectricity. Moreover, the phenomenon described here, robust spiral magnetism without a charge gap, is at the heart of one of the proposed systems where topological Majorana phases can be induced (9–14).

Finally, let us comment on our results from the perspective of the real iron-based materials. As already mentioned, a non-trivial magnetic order, such as spirals, in the vicinity of high critical temperature superconductivity can lead to topological effects. This is the case of the two-dimensional (2D) material $\text{FeTe}_{1-x}\text{Se}_x$ where zero-energy vortex bound states (Majorana fermions) have been reported (70–74). Furthermore, similar to our findings, it was argued (75) that the frustrated magnetism of $\text{FeTe}_{1-x}\text{Se}_x$ can be captured by a long-range J_1 - J_2 - J_3 spin Hamiltonian. From this perspective, it seems appropriate to assume that the phenomenon described in our work extends beyond 1D systems. Unfortunately, the lack of sufficiently reliable computational methods to treat 2D quantum models limits our understanding of multi-orbital effects in 2D. An intermediate promising route is the low-dimensional ladders from the family of 123 compounds where accurate DMRG calculations are possible. Early density functional theory and Hartree-Fock results suggest that the effects of correlations are important (37, 76) and that noncollinear magnetic order can develop in the ground state (37). The recent proposal of exploring ladder tellurides with a predicted higher value of U/W provides another avenue to consider (76). As a consequence, we encourage crystal growers with expertise in iron-based materials to explore in detail the low-dimensional family of 123 compounds, including doped samples, because our results suggest that exotic physics may come to light.

Data Availability. Computer codes used in this study are available at <https://g1257.github.io/dmrgPlusPlus/>. All data discussed in this paper are available to readers at <https://g1257.github.io/papers/104/>.

ACKNOWLEDGMENTS. We thank M. L. Baez, C. Batista, and M. Mierzejewski for fruitful discussions. J. Herbrych, A. Moreo, and E. Dagotto were supported by the US Department of Energy (DOE), Office of Science, Basic Energy Sciences (BES), Materials Sciences and Engineering Division. In addition, J. Herbrych acknowledges grant support by the Polish National Agency of Academic Exchange under Contract PPN/PPO/2018/1/00035. The development of the DMRG++ code by G.A. was supported by the Scientific Discovery through Advanced Computing (SciDAC) program funded by the US Department of Energy (DOE), Office of Science, Advanced Scientific Computer Research and Basic Energy Sciences, Division of Materials Science and Engineering, which was conducted at the Center for Nanophase Materials Science, sponsored by the Scientific User Facilities Division, Basic Energy Sciences, DOE, under contract with University of Tennessee–Battelle. J. Heverhagen and M.D. were supported by the Deutsche Forschungsgemeinschaft via the Emmy-Noether program (DA 1235/1-1) and FOR1807 (DA 1235/5-1) and by the state of Baden-Württemberg through Baden-Württemberg High Performance Computing (bwHPC). Calculations have been partly carried out using resources provided by Wroclaw Centre for Networking and Supercomputing.

- Z. G. Soos, A. Parvej, M. Kumar, Numerical study of incommensurate and decoupled phases of spin-1/2 chains with isotropic exchange J_1 , J_2 between first and second neighbors. *J. Phys. Condens. Matter* **28**, 175603 (2016).
- M. Sato, S. Furukawa, S. Onoda, A. Furusaki, Competing phases in spin-1/2 J_1 - J_2 chain with easy-plane anisotropy. *Mod. Phys. Lett.* **25**, 901 (2011).
- I. P. McCulloch *et al.*, Vector chiral order in frustrated spin chains. *Phys. Rev. B* **77**, 094404 (2008).
- M. J. P. Gingras, P. A. McClarty, Quantum spin ice: A search for gapless quantum spin liquids in pyrochlore magnets. *Rep. Prog. Phys.* **77**, 056501 (2014).
- N. Nagaosa, Y. Tokura, Topological properties and dynamics of magnetic skyrmions. *Nat. Nanotechnol.* **8**, 899 (2013).

- H. Tsunetsugu, Y. Hatsugai, K. Ueda, M. Sigrist, Spin-liquid ground state of the half-filled Kondo lattice in one dimension. *Phys. Rev. B* **46**, 3175 (1992).
- L. Balents, Spin liquids in frustrated magnets. *Nature* **464**, 119 (2010).
- I. Kimchi, A. Nahum, T. Senthil, Valence bonds in random quantum magnets: Theory and application to YbMgGaO_4 . *Phys. Rev. X* **8**, 031028 (2018).
- S. Nadj-Perge *et al.*, Observation of Majorana fermions in ferromagnetic atomic chains on a superconductor. *Science* **346**, 602 (2014).
- Y. Oreg, G. Refael, F. von Oppen, Helical liquids and Majorana bound states in quantum wires. *Phys. Rev. Lett.* **105**, 177002 (2010).
- B. Braunecker, P. Simon, Interplay between classical magnetic moments and superconductivity in quantum one-dimensional conductors: Toward a self-sustained topological Majorana phase. *Phys. Rev. Lett.* **111**, 147202 (2013).

12. J. Klinovaja, P. Stano, A. Yazdani, D. Loss, Topological superconductivity and Majorana fermions in RKKY systems. *Phys. Rev. Lett.* **111**, 186805 (2013).
13. M. Schecter, M. S. Rudner, K. Flensberg, Spin-lattice order in one-dimensional conductors: Beyond the RKKY effect. *Phys. Rev. Lett.* **114**, 247205 (2015).
14. M. Steinbrecher *et al.*, Non-collinear spin states in bottom-up fabricated atomic chains. *Nat. Commun.* **9**, 2853 (2018).
15. S. Dong, R. Yu, S. Yunoki, J.-M. Liu, E. Dagotto, Origin of multiferroic spiral spin order in the RMnO₃ perovskites. *Phys. Rev. B* **78**, 155121 (2008).
16. I. A. Sergienko, E. Dagotto, Role of the Dzyaloshinskii-Moriya interaction in multiferroic perovskites. *Phys. Rev. B* **73**, 094434 (2006).
17. S. Seki *et al.*, Correlation between spin helicity and an electric polarization vector in quantum-spin chain magnet LiCu₂O₂. *Phys. Rev. Lett.* **100**, 127201 (2008).
18. S. Furukawa, M. Sato, S. Onoda, Chiral order and electromagnetic dynamics in one-dimensional multiferroic cuprates. *Phys. Rev. Lett.* **105**, 257205 (2010).
19. Y. Tokura, S. Seki, Multiferroics with spiral spin orders. *Adv. Mater.* **22**, 1554 (2010).
20. K. Y. Povarov, Y. Feng, A. Zheludev, Multiferroic phases of the frustrated quantum spin-chain compound linarite. *Phys. Rev. B* **94**, 214409 (2016).
21. A. Scaramucci *et al.*, Multiferroic magnetic spirals induced by random magnetic exchanges. *Phys. Rev. X* **8**, 011005 (2018).
22. J. M. Caron *et al.*, Orbital-selective magnetism in the spin-ladder iron selenides Ba_{1-x}K_xFe₂Se₃. *Phys. Rev. B* **85**, 180405 (2012).
23. L. de' Medici, S. R. Hassan, M. Capone, X. Dai, Orbital-selective Mott transition out of band degeneracy lifting. *Phys. Rev. Lett.* **102**, 126401 (2009).
24. D. J. Garcia, K. Hallberg, C. D. Batista, M. Avignon, B. Alascio, New type of charge and magnetic order in the ferromagnetic Kondo lattice. *Phys. Rev. Lett.* **85**, 3720 (2001).
25. D. J. Garcia, K. Hallberg, B. Alascio, M. Avignon, Spin order in one-dimensional Kondo and Hund lattices. *Phys. Rev. Lett.* **93**, 177204 (2004).
26. J. Rincón, A. Moreo, G. Alvarez, E. Dagotto, Exotic magnetic order in the orbital-selective Mott regime of multi-orbital systems. *Phys. Rev. Lett.* **112**, 106405 (2014).
27. J. Herbrych *et al.*, Spin dynamics of the block orbital-selective Mott phase. *Nat. Commun.* **9**, 3736 (2018).
28. J. Herbrych *et al.*, Novel magnetic block states in low-dimensional iron-based superconductors. *Phys. Rev. Lett.* **123**, 027203 (2019).
29. M. Mourigal *et al.*, Block magnetic excitations in the orbitally selective Mott insulator BaFe₂Se₃. *Phys. Rev. Lett.* **115**, 047401 (2015).
30. S. Wu *et al.*, Robust block magnetism in the spin ladder compound BaFe₂Se₃ under hydrostatic pressure. *Phys. Rev. B* **100**, 214511 (2019).
31. H. Takahashi *et al.*, Pressure-induced superconductivity in the iron-based ladder material BaFe₂S₃. *Nat. Mat.* **14**, 1008 (2015).
32. M. Wang *et al.*, Spin waves and magnetic exchange interactions in the spin-ladder compound RbFe₂Se₃. *Phys. Rev. B* **94**, 041111 (2016).
33. M. Wang *et al.*, Strong ferromagnetic exchange interaction under ambient pressure in BaFe₂S₃. *Phys. Rev. B* **95**, 060502 (2016).
34. S. Artyukhin *et al.*, Solitonic lattice and Yukawa forces in the rare-earth orthoferrite TbFeO₃. *Nat. Mat.* **11**, 694 (2012).
35. M. Daghofer, A. Nicholson, A. Moreo, E. Dagotto, Three orbital model for the iron-based superconductors. *Phys. Rev. B* **81**, 014511 (2010).
36. Q. Luo *et al.*, Neutron and ARPES constraints on the couplings of the multiorbital Hubbard model for the pnictides. *Phys. Rev. B* **82**, 104508 (2010).
37. Q. Luo *et al.*, Magnetic states of the two-leg-ladder alkali metal iron selenides AFe₂Se₃. *Phys. Rev. B* **87**, 024404 (2013).
38. M. Yi, Y. Zhang, Z.-H. Shen, D. Lu, Role of the orbital degree of freedom in iron-based superconductors. *NPJ Quantum Materials* **2**, 57 (2017).
39. N. D. Patel *et al.*, Fingerprints of an orbital-selective Mott phase in the block magnetic state of BaFe₂Se₃ ladders. *Commun. Phys.* **2**, 64 (2019).
40. K. Haule, G. Kotliar, Coherence-incoherence crossover in the normal state of iron oxypnictides and importance of Hund's rule coupling. *New J. Phys.* **11**, 025021 (2009).
41. Z. P. Yin, K. Haule, G. Kotliar, Kinetic frustration and the nature of the magnetic and paramagnetic states in iron pnictides and iron chalcogenides. *Nat. Mat.* **10**, 932 (2011).
42. J. Ferber, K. Foyevtsova, R. Valentí, H. O. Jeschke, LDA + DMFT study of the effects of correlation in LiFeAs. *Phys. Rev. B* **85**, 094505 (2012).
43. Y.-Z. Zhang *et al.*, General mechanism for orbital selective phase transitions. *Phys. Rev. B* **85**, 035123 (2012).
44. S. R. White, Matrix formulation for quantum renormalization groups. *Phys. Rev. Lett.* **69**, 2863 (1992).
45. U. Schollwöck, The density-matrix renormalization group. *Rev. Mod. Phys.* **77**, 259 (2005).
46. G. Alvarez, The density matrix renormalization group for strongly correlated electron systems: A generic implementation. *Comput. Phys. Commun.* **180**, 1572 (2009).
47. S. R. White, Density matrix renormalization group algorithms with a single center site. *Phys. Rev. B* **72**, 180403 (2005).
48. E. Jeckelmann, Dynamical density-matrix renormalization-group method. *Phys. Rev. B* **66**, 045114 (2002).
49. H. Benthein, E. Jeckelmann, Spin and charge dynamics of the one-dimensional extended Hubbard model. *Phys. Rev. B* **75**, 205128 (2007).
50. A. Nocera, G. Alvarez, Spectral functions with the density matrix renormalization group: Krylov-space approach for correction vectors. *Phys. Rev. E* **94**, 053308 (2016).
51. T. D. Kühner, S. R. White, Dynamical correlation functions using the density matrix renormalization group. *Phys. Rev. B* **60**, 335 (1999).
52. T. Hikihara, M. Kaburagi, H. Kawamura, T. Tonegawa, Ground state phase diagram of frustrated S = 1 XXZ chains: Chiral ordered phases. *J. Phys. Soc. Jpn.* **69**, 259 (2000).
53. T. Hikihara, M. Kaburagi, H. Kawamura, Ground-state phase diagrams of frustrated spin-S XXZ chains: Chiral ordered phases. *Phys. Rev. B* **63**, 174430 (2001).
54. J. C. Xavier, R. G. Pereira, E. Miranda, I. Affleck, Dimerization induced by the RKKY interaction. *Phys. Rev. Lett.* **90**, 247204 (2003).
55. M. F. Maghrebi, Z.-X. Gong, A. V. Gorshkov, Continuous symmetry breaking in 1D long-range interacting quantum systems. *Phys. Rev. Lett.* **119**, 023001 (2017).
56. B. S. Shastry, Exact solution of an S = 1/2 Heisenberg antiferromagnetic chain with long-range interactions. *Phys. Rev. Lett.* **60**, 639 (1988).
57. F. D. M. Haldane, Exact Jastrow-Gutzwiller resonating-valence-bond ground state of the spin-1/2 antiferromagnetic Heisenberg chain with 1/r² exchange. *Phys. Rev. Lett.* **60**, 635 (1988).
58. A. W. Sandvik, Ground states of a frustrated quantum spin chain with long-range interactions. *Phys. Rev. Lett.* **104**, 137204 (2010).
59. N. Laflorencie, I. Affleck, M. Berciu, Critical phenomena and quantum phase transition in long range Heisenberg antiferromagnetic chains. *J. Stat. Mech.*, 10.1088/1742-5468/2005/12/P12001 (2005).
60. Z.-H. Li, A.-M. Wang, Matrix product state approach to a frustrated spin chain with long-range interactions. *Phys. Rev. B* **91**, 235110 (2015).
61. H. Ueda, S. Onoda, Vector-spin-chirality order in a dimerized frustrated spin-1/2 chain. *Phys. Rev. B* **89**, 024407 (2014).
62. H. Onishi, Magnetic excitations of spin nematic state in frustrated ferromagnetic chain. *J. Phys. Soc. Jpn.* **84**, 083702 (2015).
63. P. Bak, Commensurate phases, incommensurate phases and the devil's staircase. *Rep. Prog. Phys.* **45**, 587 (1982).
64. M. Kataoka, Spin waves in systems with long period helical spin density waves due to the antisymmetric and symmetric exchange interactions. *J. Phys. Soc. Jpn.* **56**, 3635 (1987).
65. J. Jensen, A. R. Mackintosh, *Rare Earth Magnetism: Structures and Excitations* (Clarendon Press, 1991).
66. M. Mochizuki, Spin-wave modes and their intense excitation effects in skyrmion crystals. *Phys. Rev. Lett.* **108**, 017601 (2012).
67. N. Stüsser, U. Schotte, A. Hoser, M. Meissner, Field-distorted magnetic spiral structure of CsCuCl₃. *Physica B* **350**, E47 (2004).
68. G. W. Winkler, M. Ganahl, D. Schuricht, H. G. Evertz, S. Andergassen, Interaction effects in a microscopic quantum wire model with strong spin-orbit interaction. *New J. Phys.* **19**, 063009 (2017).
69. X. Li, E. Zhao, W. V. Liu, Topological states in a ladder-like optical lattice containing ultracold atoms in higher orbital bands. *Nat. Commun.* **4**, 1523 (2012).
70. P. Zhang *et al.*, Observation of topological superconductivity on the surface of an iron-based superconductor. *Science* **360**, 182 (2018).
71. D. Wang *et al.*, Evidence for Majorana bound states in an iron-based superconductor. *Science* **362**, 333 (2018).
72. P. Zhang *et al.*, Multiple topological states in iron-based superconductors. *Nat. Phys.* **15**, 41 (2018).
73. T. Machida *et al.*, Zero-energy vortex bound state in the superconducting topological surface state of Fe(Se,Te). *Nat. Mat.* **18**, 811 (2019).
74. R.-X. Zhang, W. S. Cole, S. Das Sarma, Helical hinge Majorana modes in iron-based superconductors. *Phys. Rev. Lett.* **122**, 187001 (2019).
75. H. Ruiz *et al.*, Frustrated magnetism from local moments in FeSe. *Phys. Rev. B* **99**, 125130 (2019).
76. Y. Zhang, L.-F. Lin, A. Moreo, S. Dong, E. Dagotto, Magnetic states of iron-based two-leg ladder tellurides. *Phys. Rev. B* **100**, 184419 (2019).